# Selective Laser Melting of Alumina: A Single Track Study

Zhiqi Fan, Mingyuan Lu, Han Huang

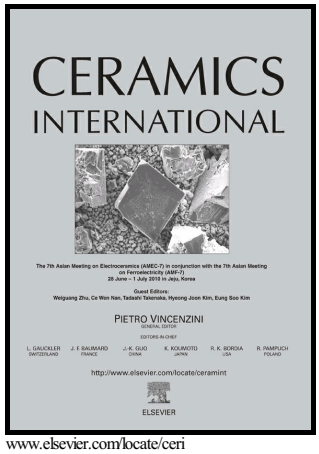


www.elsevier.com/locate/ceri

PII: S0272-8842(18)30477-2
DOI: https://doi.org/10.1016/j.ceramint.2018.02.166
Reference: CERI17568

To appear in: *Ceramics International*

Received date: 11 December 2017
Revised date: 20 February 2018
Accepted date: 20 February 2018

Cite this article as: Zhiqi Fan, Mingyuan Lu and Han Huang, Selective Laser Melting of Alumina: A Single Track Study, *Ceramics International,* https://doi.org/10.1016/j.ceramint.2018.02.166

# Selective Laser Melting of Alumina: A Single Track Study

Zhiqi Fan, Mingyuan Lu*, Han Huang

*School of Mechanical and Mining Engineering, University of Queensland, QLD 4072, Australia*

*Corresponding author. School of Mechanical and Mining Engineering, The University of Queensland, St Lucia, QLD 4072, Australia; mingyuan.lu@uqconnect.edu.au;*



## Abstract

Ceramics-based additive manufacturing is a complex process and the solidification mechanism and microstructural evolution are currently not fully understood. In this work, $Al_2O_3$ single tracks were formed using a customised selective laser melting (SLM) system equipped with a high power diode laser. The effects of laser energy density (LED) on geometry, microstructure and micro-mechanical properties of $Al_2O_3$ tracks were investigated. To better understand the solidification mechanism, a transient three-dimensional thermal model was developed for predicting the thermal behaviour of the melt pool. The results indicated the use of high LED gave rise to decreased viscosity and surface tension of the molten alumina and led to localised melting of the substrate. Both, in turn, enabled the formation of a continuous solidified track. The solidified tracks were primarily composed of columnar dendrite. When relatively high LED ($\geq$25.7 kJ/m) was applied, equiaxed dendrite appeared along the central line near the

track surface. The size of dendritic grains decreased with the decreased LED, attributed to the increased cooling rate at solidification interface. The micro-hardness of the solidified track was found to be inversely proportional to the grain size owning to grain boundary strengthening effect.

**Keywords**: Alumina; Selective laser melting; Solidification; Laser energy density



# 1. Introduction

Alumina ($Al_2O_3$) is one of the most widely used and versatile engineering ceramics, owing to its high-temperature strength, high hardness, superior wear and corrosion resistance, low density, and bio-inertness [1]. Alumina based ceramics have been widely used to make devices and components applied in automotive and aviation industries, machining tools as well as medical implants. Conventional forming methods, including die pressing, slip casting, extrusion and injection moulding, are used to produce alumina ceramics net-shape components. These techniques, however, are commonly followed by high temperature sintering and final machining/finishing processes in order to deliver the desired component shape with precision [2, 3]. Shrinkage in the course of sintering often leads to part distortion and low geometric accuracy [4]. And final machining generally requires diamond tooling [5], which is costly and time-consuming. Many of those processes can represent up to 80% of the overall manufacturing cost of a ceramic product [6].

Selective laser melting (SLM) technique is a promising process for forming components with complex shape. In a SLM process, 3D objects are built by selectively fusing powder particles using a focused laser beam in a layer by layer fashion, directly from a computer aided design (CAD) model [7]. SLM has been widely applied in forming metal and polymer parts, whilst SLM for ceramics is still at the very early stage and faces great challenges due to their high melting point, low thermal conductivity, low thermal shock resistance and inherent brittleness [7, 8]. However, the application of SLM into manufacturing of ceramic products has been recently driven by the increasingly higher demand for ceramic parts with complex shapes for high performance application [9].

Previous studies on SLM of ceramics were mainly concerned with the development of different strategies for improving laser-powder interaction to achieve high density and defect free parts. Effective approaches include the use of laser absorptivity enhancement additives [10], preheating [11] and special powder formulation with a eutectic mixture (i.e. alumina-zirconia) [2, 12]. In SLM, the quality of the 3D objects is dependent on the geometrical stability and site-specific microstructure of each scanned line [13, 14]. To produce a part with high density and minimal manufacturing defects, the effects of laser processing conditions on the geometries of a single track must also be well understood. In addition, rapid cooling and high thermal gradient associated with single track formation often result in unique heterogeneous microstructure hence anisotropic and varied mechanical properties within the solidified track [15, 16]. However, till now in-depth understanding of the relationship between process conditions and microstructural evolution of ceramic materials processed using SLM is lacking.

In this study, alumina single tracks were formed on α-alumina substrates using a high energy diode laser (HPDL). The role of laser energy intensity in terms of laser energy density (LED) in single track formation was systematically investigated. The relationships between the geometry, microstructure and mechanical property of a single track and LED were explored systematically. A finite volume method based model was also developed to simulate the thermal behaviour of the melt pool in SLM process, which was validated using the experimental results.

# 2. Methodology

## 2.1. Experiment

### 2.1.1. Materials

The powder used in this study was atomised α-$Al_2O_3$ powders (99.8% purity) supplied by Inno-Trust Tech Co. Ltd, Taiwan. As shown in Fig. 1, the powder particles have spherical shapes and the average particle size was 20 μm. The apparent density of the powder was approximately 40%. Bulk alumina plates (92% purity, supplied by MULTOTEC Australia) were used as substrates. Prior to laser melting, the alumina powder was manually spread onto the substrate, and the thickness of the powder layer was controlled at approximately 250 μm.

### 2.1.2. Selective laser melting

Alumina single tracks were formed on the substrates using a customized SLM facility shown in Fig. 2. This system consisted of a 2 kW continuous fibre coupled diode laser (Laserline 2000, Germany), a three-axis motorized stage and a PC controller. The laser beam has a wavelength of 980 nm, a spot size of 1.2 mm and a "top-hat" beam intensity profile. The laser power ($P$) and scanning velocity ($v$) varied from 100 to 400 W with a

50 W interval and 300 to 1000 mm/min with a 100 mm/min interval respectively. To characterize the combined effect of $P$ and $v$ in SLM, laser energy density (LED, kJ/m) was used to characterise the intensity of laser energy input, which is defined as [17]:

$$LED = P / v \quad (1)$$

### 2.1.3. Characterization

The morphology and microstructure of the powder material and solidified tracks were characterized using a scanning electron microscope (SEM, JEOL, JSM-7100F, Japan) and a confocal optical microscope (OM, Olympus, LEXT OLS4100, Japan). For preparing cross-sectional samples, the solidified tracks were sectioned using a M1D15 diamond saw (Struers, Denmark). The specimens were then embedded in epoxy resin using hot-mounting process and polished for metallographic examination.

Grain size of the solidified materials was quantified using the linear intercept method according to the ASTM E112-96 standard [18]. For columnar dendritic grains, the primary dendrite arm spacing (PDAS), which is defined as the distance between two adjacent dendrite tips, was measured. For each sample, ten measurements were made on selected regions and the results were averaged for comparison. Microhardness tests were conducted on the polished cross-sections at room temperature using a Vickers microhardness tester (Struer, Denmark). The applied load was 2 N and holding time was 12 seconds.

## 2.2. Numerical modelling

### 2.2.1. The heat transfer mechanism

The interaction between incident laser and alumina powders in a SLM process is a complex physical and metallurgical process. When a laser beam irradiates on the surface of a powder bed, a significant part of the laser energy is back-scattered into the surrounding atmosphere. The remaining concentrated flux of energy will penetrate into the powder bed via absorption, transmission and forward scattering. A localized molten pool is then formed, which is bonded with the substrate or the previously consolidated layer. The in-process heat transfer is controlled by thermal conduction, convection and radiation. In the thermal model used in this study, all the three heat transfer mechanisms were taken into account.

### 2.2.2. Finite volume method (FVM) model

*The geometric model and meshing*

A 3D finite volume method (FVM) model was developed using the FLUENT® software (ANSYS Inc, US) for thermal conditions prediction. The model was symmetrical with respect to the x-z plane. A half-symmetry model was used in order to reduce computation time, as shown in Fig. 3. In the model, dimensions of the powder layer and alumina substrate were $7\times1.5\times0.25$ mm$^3$ and $7\times1.5\times0.55$ mm$^3$ respectively. The powder bed was meshed using a uniformly structured meshing method with hexahedral cells of 50 μm in size. The substrate was meshed using a sweep method, in which the minimum size of the hexahedral cell used was 70 μm and the sweep bias was 2.

To make the complex thermal problem tractable mathematically, the following assumptions were applied: (1) the laser energy source had a uniform energy distribution

(i.e. a top-hat profile); (2) the entire powder bed was a homogeneous and continuous medium during thermal transmission; (3) heat transfer due to Maragoni convection was neglected; (4) the molten pool was flat, and the shrinkage during powder melting was not considered; (5) mass and heat loss due to vaporization was neglected.

*Governing equation, initial and boundary conditions*

The heat conduction transfer in SLM process was implemented into the FVM thermal model using the governing equation [19]:

$$\rho c\frac{\partial T}{\partial t}=\frac{\partial}{\partial x}\left(k\frac{\partial T}{\partial x}\right)+\frac{\partial}{\partial y}\left(k\frac{\partial T}{\partial y}\right)+\frac{\partial}{\partial z}\left(k\frac{\partial T}{\partial z}\right)+Q \quad (2)$$

where $\rho$ is the density (kg/m$^3$), $c$ the specific heat (J/kg K), $T$ the temperature (K), and $k$ is the thermal conductivity (W/m K) of the powder material, $t$ is time (s), and $Q$ is the rate of internal energy conversion per unit volume (W/m$^3$). The initial temperature distribution for powder-substrate system at $t$ = 0 was treated to be uniform, which was expressed as:

$$T(x,y,z,t)\big|_{t=0}=298\,K \quad (3)$$

The boundary condition applied on the top surface of the powder bed was given by:

$$-k\frac{\partial T}{\partial n}=h(T-T_0)+\sigma\varepsilon(T^4-T_0^4)+q \quad (4)$$

where $T$ is the surface temperature of the powder bed, $n$ is the normal vector of powder surface, $T_0$ is ambient temperature, $\varepsilon$ is emissivity, $\sigma$ is the Stefan-Boltzmann constant, $h$ is the thermal convection coefficient (W/m$^2$ K), and $q$ is the input heat flux (W/m$^2$).

*The volumetric heat source model*

The optical properties of $Al_2O_3$ are distinct from those of metallic materials with respect to near infrared (NIR) wavelength. While the interaction between NIR laser beam and metallic powder are restricted to the vicinity of powder bed surface, the NIR laser radiation could penetrate much deeper inside $Al_2O_3$ powder media owning to the high optical transparency and reflectivity of $Al_2O_3$ [20]. Thus, laser absorption of $Al_2O_3$ powder could not be simply modelled as a surface heat flux, and the travel distance of laser beam along *z* axis in alumina powder medium should be taken into accounted. The volumetric heat source, which considered laser input spatial distribution, could be used in this case, which was described by the Beer-Lamberts law [21]:

$$q_v(x,y,z) = (1-R)\alpha I_0(x,y)e^{-\alpha z} \tag{5}$$

where $R$ is the surface reflectivity of alumina, $I_0$ is the collimated laser flux at the top surface and $\alpha$ is the absorption coefficient of alumina powders, which could be estimated using [20]:

$$\alpha = \alpha_0(1-\varphi) \tag{6}$$

where $\alpha_0$ is the absorption coefficient of $Al_2O_3$ bulk material, $\varphi$ is the porosity of the powder bed. $I_0$ is the collimated laser flux at the top surface. Since a top-hat laser was utilized in this work, the laser energy was considered to be uniformly distributed within the spot size. The collimated laser heat flux $I_0$ was thus modelled as:

$$I_0 = P/(\pi r^2) \tag{7}$$

where $P$ is the laser power, and $r$ is the radius of laser beam. During a SLM process, the heat source moved along the $x$-axis at a pre-set scan speed. The laser deposition region at time $t$ was defined as:

$$(x - x_s - vt)^2 + (y - y_s)^2 \le r^2 \quad (8)$$

where ( $x_s$ , $y_s$ ) is the coordinates of the initial position of the laser beam centre (at $t$=0). The laser energy deposition outside this area was set to zero during each time step.

*The thermal properties used in the model*

Due to rapid temperature change in SLM, temperature-dependent thermal properties of the powder material need to be well defined in the numerical models. Fig. 4 shows the dependence of thermal conductivity and specific heat capacity of bulk alumina on temperature. The thermal conductivity of a powder material is affected by factors including porosity, laser wavelength, packing structure, and size and morphology of the powder particles [22, 23]. The effective thermal conductivity of the powder bed can be estimated using [24]:

$$\frac{k_{eff}}{k_f} = \left(1 - \sqrt{1-\varphi}\right)\left(1 + \frac{\varphi k_r}{k_f}\right) + \sqrt{1-\varphi}\left[\frac{2}{1-\frac{k_f}{k_s}}\left(\frac{1}{1-\frac{k_f}{k_s}}\ln\left(\frac{k_s}{k_f}\right) - 1\right) + \frac{k_r}{k_f}\right] \quad (9)$$

where $\varphi$ is the porosity of the powder material, $k_s$ is the thermal conductivity of the bulk material and $k_f$ is the thermal conductivity of the ambient atmosphere and $k_r$ is the thermal conductivity due to the radiation among particles in the powder bed, which is expressed as:

$$k_r = 4F\sigma T_p^3 D_p \quad (10)$$

in which σ is the Stefan-Boltzman constant, $D_p$ is the mean diameter of powder particles, $T_p$ is the temperature of the particles, and $F$ is a view factor, taken as 1/3. Other physical properties of alumina material used in this model are listed in Table 1.

*Phase transformations in the SLM process*

In a SLM process, powder particles were melted when they encountered the high-energy laser radiation, and then the melt solidified in subsequent cooling. Thus, the latent heat of melting need to be taken into consideration for simulating the free energy involved in the solid to liquid and liquid to solid phase transformations. To define the latent heat, enthalpy can be expressed as a function of temperature [34]:

$$H = \int \rho c dT + \Delta H_{liquid} \quad (11)$$

where $\rho$ is the density and $c$ is the specific heat capacity of alumina, $T$ is the temperature, and $\Delta H_{liquid}$ is the latent heat of melting ( $\Delta H_{liquid}$ =0 when $T<2327\ K$).

The user defined memory function (UDMI) in FLUENT® was utilized to identify if the temperature of each cell exceeded the melting point at each time step in the recorded thermal history. UDMI imposed a threshold for determining the occurrence of phase change from solid (powder) to liquid during heating and liquid to solid (consolidated bulk material) during cooling. The instantaneous molten pool was isolated from the surrounding solid using the 2327 K isotherm and the 3D shape of the melt pool can thus be identified and characterized.

# 3. Results from SLM Experiments

## 3.1. Process map

The process map of $Al_2O_3$ single tracks is shown in Fig. 5. Three different types of tracks were identified, including continuous (A), discontinuous (B), and balled (C) tracks. When the laser power used was less than 100 W and the scanning speed was higher than 500 mm/min, laser-powder coupling did not occur due to insufficient energy input (D). Broken single tracks in Zones B and C were formed attributed to instable melt flow behaviour or balling. Further increase in laser power or decrease in scan speed led to the formation of stabilized and continuous tracks in Zone A and the minimum laser energy density (LED) for obtaining a continuous track was 13.3 kJ/m.

## 3.2. Track geometry

Fig. 6 shows the effects of LED on the geometry and dimensions of single tracks. The cross-section profile of a track is defined using width $w$, depth $d$ and contact angles $\theta$, as shown in Fig. 6 (a). It should be noted that the samples being measured were selected from those in Zone A in Fig. 5, i.e. $P$ was in the range of 200 - 400 W and $v$ varied between 500 and 900 mm/min. The resulted LED was thus in the range of 13.3 - 48 kJ/m. As shown in Fig. 6 (b), the track width $w$ increased monotonically with the increase in LED, ranging from 1198 μm (at 13.3 kJ/m LED) to 1763 μm (at 48 kJ/m LED). Similarly, the track depth $d$ increased with the increase in LED, varying from 261 μm (at 13.3 kJ/m LED) to 513 μm (at 48 kJ/m LED), as shown in Fig. 6 (c). Fig. 6 (d) shows that the contact angle $\theta$ decreased from 32.4° to 16.4° as the LED increased from 13.3 kJ/m to 48 kJ/m.

## 3.3. Microstructure

### 3.3.1 Top surface

Fig. 7 shows the top-surface microstructure of typical single tracks. Two areas of interest were examined at high magnifications. They were Zone I, an area within the track adjacent to the edge (shown in a-2, b-2, c-2) and Zone II at the centre of the track (shown in a-3, b-3, c-3). Two distinct crystalline structures with a range of scales were identified, which were columnar and equiaxial dendrites, marked as C and E, respectively, in Fig. 7. It's apparent that the size of both types of grains increased with the increase of LED. The size of the columnar dendrites in Zone I were compared in Figs. 7 (a-2) to (c-2). It was found that the value of PDAS increased from 2.22 μm (13.3 kJ/m LED, (a-2)) to 4.01 μm (48 kJ/m LED, Fig. 7(c-2)) with the increasing magnitude of LED. In Zone II, a noticeable transition from columnar dendrite to equiaxial dendrite was observed. For the track formed using relatively low LED (13.3 kJ/m, Fig. 7 (a-3)), only fine columnar dendritic grains was observed. In the track formed using LED of 25.7 kJ/m, a mixture of columnar and equiaxial dendrites were found, as demonstrated in Fig. 7 (b-3). Fig. 7 (c-3) exhibits large and distinctive equiaxial dendrite populated in the centre of the track that formed using LED of 48 kJ/m.

### 3.3.2 Cross-section

Fig. 8 (a) shows a typical cross sectional view of a single track (produced using process conditions of 25.7 kJ/m, 300 W, 700 mm/min). The growth of columnar dendrites took place at the track-substrate boundary and developed towards the top central area. High magnification images of regions L1-L5 in Fig. 8 (a) are shown in Figs. 8 (b)-(f), respectively. Along the vertical L1-L2-L3 path (from the top to the bottom along the vertical central line), an increasing trend in grain size was found; and their PDAS values

measured were 4.11 μm, 4.19 μm and 4.24 μm for L1, L2 and L3 respectively. Along the horizontal L5-L4-L2 path, the grain size of the columnar dendrites decreased gradually from the centre (L2) towards the edge of the track (L5), with the PDAS values being 4.4 μm, 3.58 μm and 3.1 μm, for L2, L4 and L5, respectively.

The average PDAS values of columnar dendrites in different regions of the track cross-section (L1-L5 in Fig. 8 (a)) were measured and plotted as a function of LED in Fig. 9. The value of PDAS was found proportional to the level of LED. The minimum PDAS was 2.35 μm when the LED was 13.3 kJ/m, and the maximum PDAS was 5.98 μm when LED of 48 kJ/m was applied, clearly indicating the grain coarsening effect as a result of the increase of LED. In addition, the PDAS of the dendrites in the centre (L1-L3) was found consistently greater than that in the area closer to the track edge (L4 and L5).

### 3.4. Microhardness

Microhardness was measured at different locations of the single tracks' cross-sections (zones L1-L5 in Fig. 8), and the averaged values were plotted as a function of LED in Fig. 10. It is seen that the hardness value was within the range of 15.4-19.9 GPa. The averaged hardness appeared to slightly decrease with the increase of LED. The maximum was 18.3 GPa at LED of 20 kJ/m, while the minimum was 16.3 GPa at LED of 34.3 kJ/m.

## 4. Simulation results

### 4.1. Temperature distribution

Fig. 11 (a) shows the transient temperature distribution in the melt pool region when the incident laser moved along x-axis, which resulted in an elongated horizontal contour.

The maximum temperature (3893 K) was found in the melt track front locating on the x-axis, which was slightly higher than the boiling temperature of alumina (3700 K) [35]. It should be noted that the location of maximum temperature did not coincide with the centre of the laser spot. It can be seen in Figs. 11 (b) and 11 (c) that the laser spot centre (dashed line, x=0.0048 m) was slightly ahead of the temperature maxima. This was likely due to the combination of heat accumulation effect and the change of thermal conductivity as a result of powder to solid transition [34]. In addition, the thermal gradient of the scanning front was much greater than that of the tail region, which was also attributed to the thermal conductivity change during the transition of loose powder to dense solid [19]. The shape of molten pool is shown in Fig. 11 (d) the dimension of the molten pool is defined using length ($l$), depth ($d$) and half width ($w_{half}$, $w=2w_{half}$).

Fig. 12 shows the temperature distributions along different axes of y and z, plotted as a function of LED. All the curves were originated from the temperature maxima at top surface (when y = 0, z = 0), and the LED being applied was in the rang of 13.3-48 kJ/m. As shown in Fig. 12, the temperature at any given location increased with the increase of LED. In particular, the maximum temperature increased from 3112 K at 13.3 kJ/m LED to 5192 K at 48 kJ/m LED. The temperature decreased with the increased distance from the centre and a steep temperature drop were found in all curves before they reached a plateau in the end.



### 4.2. Molten pool geometry

Fig. 13 shows the influence of LED on molten pool geometry, It was seen that a higher LED led to the increases in $d$, $w$ and $l$ from 211, 1120 and 1659 $\mu m$ (LED = 13.3 kJ/m) to 494, 1482 and 3385 $\mu m$ (LED = 48 kJ/m), respectively. In order to validate the numerical models, the dimensions ($d$ and $w$) of the calculated molten pool were

compared with that obtained experimentally (i.e. the data in Fig. 6). As shown in Fig. 13, the simulation results agree well with the experimental measurements. It was also found that the simulated molten pools were slightly shallower and narrower than the experimental ones. This discrepancy could be caused by the fact that (1) the abrupt increase of absorption coefficient [36] at elevated temperature was not considered in this model; and (2) material removal due to evaporation was not taken into account in the current model.

### 4.3. Solidification parameters

The metallurgical structure of the solidified tracks are dependent on two fundamental solidification parameters, namely thermal gradient $G$ (K/m) and solidification rate $R$ (m/s). The cooling rate, defined as $C=GR$ (K/s), determines the grain size. In general, the higher the cooling rate is, the finer the grains become [37]. The magnitude of $G$ and $R$ can be calculated using [38]:

$$G = \sqrt{\left(\frac{\partial T}{\partial x}\right)^2 + \left(\frac{\partial T}{\partial y}\right)^2 + \left(\frac{\partial T}{\partial z}\right)^2} \tag{12}$$

$$R = v\cos(\alpha) \tag{13}$$

$$\cos(\alpha) = \frac{-\frac{\partial T}{\partial x}}{G} \tag{14}$$

where $\frac{\partial T}{\partial x}, \frac{\partial T}{\partial y}, \frac{\partial T}{\partial z}$ are respective temperature gradients along $x$, $y$, $z$ directions, $v$ is the laser scan speed, and $\alpha$ is the angle between scan direction and solidification growth direction.

In order to explore the effect of LED on the solidification parameters, the values of $G$, $R$, and $C$ of the liquid-solid interface of the molten pool were calculated using Eqs. (12) to (14). The mean values ($G_m$, $R_m$, and $C_m$ respectively) were plotted in Fig. 14 against the level of LED. As shown in Fig. 14 (a), $G_m$ decreased as LED increased, with the maximum being $2.895\times10^6$ K/m at LED of 13.3 kJ/m and the minimum being $2.064\times10^6$ K/m at LED of 48 kJ/m. The relationship between $R_m$ and LED was shown in Fig. 14 (b). The value of $R_m$ decreased from 0.00484 m/s to 0.00169 m/s with the increase of LED. Fig. 14 (c) shows that $C_m$ decreased with the increase in LED, with the maximum value being 7038.2 K/s at the LED of 13.3 kJ/m and the minimum value being 1704.7 K/s at the LED of 48 kJ/m.

## 5. Discussion

Plateau-Rayleigh instability of a molten track [39] is driven by high surface tension forces. Therefore, a melt pool with high length-to-width ratio tends to break off into smaller entities, attempting to reduce surface energy [40]. The lack of metallurgical bonding between the melt and the substrate can also lead to breakup of a melt pool [41]. Sufficient substrate remelting is crucial in stabilizing the melt pool [39, 41], which can be achieved by properly increasing laser energy. When the incident laser energy is insufficiently great to melt both the powder layer and the substrate, the melt is prone to coalesce and form a string of disconnected melt beads to reduce surface energy. Our experiment and simulation results clearly indicated that LED significantly affects the geometries of scanned tracks. As shown in Fig. 5, the use of relatively high LED favours the formation of continuous track. In this work, the minimum LED for attaining a continuous track was found to be 13.3 kJ/m, below which discontinuous and balled tracks were generated.

The cross-sections of the continuous tracks were relatively shallow and wide. The increase in LED increased the volume of the melt, which in turn widened and deepened the solidified tracks (see Figs. 6 (b) and (c)). The contact angle, on the contrary, exhibited a downward trend as LED increased (see Fig. 6 (d)). With a higher LED, more energy was supplied to the molten alumina, which resulted in higher melt pool temperature (see Fig. 12). The increase of temperature subsequently led to the reduction of both viscosity and surface tension of the melt [42]. As a result, wetting of the substrate was enhanced, manifested by the decrease of contact angle [15, 43].

Rapid heating and cooling associated with the SLM process led to the formation of alumina tracks with unique solidified microstructures, as the cooling rate and temperature gradient varied considerably across the moving melt pool. The microstructure of the solidified tracks differed significantly from those obtained using conventional powder metallurgy methods. For examples, the microstructure of alumina parts fabricated using conventional powder metallurgy method is comprised of primarily equiaxial grains [44]. In this work, columnar dendrites were found to be the predominant microstructural feature in the solidified tracks by SLM, as can be seen in Fig. 7 (top view) and Fig. 8 (cross-sectional view. This unique grain shape anisotropy of a single track will inevitably result in anisotropic mechanical property of a SLM alumina part. Hence, the understanding of the microstructure evolution in the course of the solidification process is essential. This can also provide valuable guidance to optimize the load bearing capability of a 3D part in a particular application by taking advantage of the property anisotropy. This is particularly valuable for manufacturing alumina parts used for medical applications such as orthopedic implants, in which the

grain orientation of the implant material should be aligned with or correlated to the stress tensors.

In the SLM process, solidification occurred at the fusion boundary (solid-liquid interface) by means of epitaxial growth on the partially melted grains in the substrate [37]. Columnar dendrites grew in an adverse direction to that of the heat flow. The heat flew approximately from the central top region to the substrate/solidified track boundary owing to rapid heat dissipation of the substrate. When LED was higher than 25.7 kJ/m, equiaxial dendrites started to form at the central region near the surface of the solidified track (see Fig. 7b-3 and Fig. 7c-3). Analogous grain structures were also reported and discussed in laser surface processing of $Al_2O_3$ [45]. The formation of equiaxial dendritic grains at relatively high LED could be attributed to the nucleation induced by rapid cooling at molten pool surface [46]. When high LED was applied, both radiative and evaporative heat loss occurred at the melt pool surface was intensified, which resulted in localized high cooling rate. Stable nuclei were then formed in the undercooled melt and the subsequent nuclei growth led to the formation of equiaxed dendritic grains [47]. The growing columnar dendrites originated from the fusion boundary eventually met the equiaxed grains near the centre of the track when the solidification process came to an end. As a result, two distinctive microstructural features were observed in the solidified single track formed using relatively high LEDs.

The grain sizes also exhibited a dependence on the magnitude of LED used, as shown in Fig. 9. The increase in LED led to the decrease of averaged cooling rate $C_m$ at solid-liquid interface, as shown in Fig. 14 (c). Since a higher cooling rate is often associated with finer microstructure, higher LED resulted in larger grain sizes, as anticipated. The grain size, in turn, affected the hardness of the tracks. It was found that the micro-

hardness values of the tracks slightly increased with the reduction of LED, as shown in Fig. 10. The relation between grain size and hardness can be described using the Hall-Petch relation [48]:

$$H = H_0 + kD^{-1/2} \quad (15)$$

where $H$ is the hardness of the polycrystalline material, $H_0$ is the hardness of a single crystal, $k$ is a constant and $D$ is the grain size. This equation gives an empirical description of grain boundary strengthening effect in materials [48]. The micro-hardness data was fitted using eq. 15 and the best fitting regression equation was $y = 9.221x + 12.55$ with $R$-squared value of 0.911, as shown in Fig. 15. The hardness value is almost linearly proportional to the inverse square root of PDAS, indicating that the reduction of LED hardened the alumina tracks via grain refinement.

The selection of laser source could also have substantial influence on the consolidation of ceramic powders, because the laser absorptivity of a powder material is dependent on laser wavelength and the metallurgical behaviour of the powder in melting. Commercially available SLM/SLS machines typically use $CO_2$ and Nd:YAG lasers. In this study, a high power diode laser (HPDL) was utilized. The key advantages of applying HPDL laser in material processing include uniform melting/heating zones, smooth surface, process consistency and repeatability [49]. These features are primarily attributed to the inherent beam stability and uniform laser energy distribution of a HPDL laser [50]. The wavelength of a HPDL laser (0.98 μm) locates in the NIR region of the electromagnetic spectrum. In general, an incident light within this spectral range is weakly-absorbed and highly-reflected by bulk $Al_2O_3$ [20, 28]. This seems contradicting the findings in a number of studies, reporting that the radiation of a NIR

laser could supply sufficient energy to fuse $Al_2O_3$ porous material [51]. In this study, the minimum LED required for melting $Al_2O_3$ powder was only 9 kJ/m (i.e. in Zone C in Fig 5), which is much smaller than the energy required for melting bulk $Al_2O_3$ substrate (330 kJ/m). Such finding indicates that the laser absorptivity of powdered $Al_2O_3$ is much higher than that of bulk $Al_2O_3$. This could be due to the enhanced penetration of HPDL laser rays in powder medium and multiple scattering effect. When the incident radiation energy deposited onto the powder surface, the laser rays penetrated the highly porous powder media and interacted with sub-surface particles via multiple scattering. The multiple scattering effect subsequently led to improved laser absorption, which was verified both numerically [52] and experimentally [53]. The enhanced laser absorption of powders therefore makes HPDL laser competitive in the powder-bed-based AM applications, which should be an ideal energy source for processing ceramic powders. In addition, HPDL laser also has economic benefits, such as high energy conversion efficiency, low operating cost, and long service life [49, 50].



## Conclusions

Consolidated alumina tracks were fabricated by means of SLM using a HPDL laser. The effects of LED on the geometry, microstructure and hardness of the tracks were investigated. It was found that higher laser power and lower scan speed enabled the formation of stabilized melt pool and thus continuous solidified tracks, due to the reduced viscosity and surface tension of the alumina melt and the enhanced melting of the substrate. The increase in LED led to the increases in width and depth of the solidified tracks, but the decrease of their contact angles.

The primary microstructural feature in the solidified tracks was columnar dendrite. The size of the columnar dendrites increased with the increased LED, which was attributed to the decrease of cooling rate at solidification interface. A higher cooling rate was associated with the formation of finer microstructure. Lower LED resulted in smaller grain sizes, which in turn increased the hardness of the tracks. When a relatively high LED of 25.7 kJ/m was applied, equiaxed dendrites were formed at the centre of the solidified track near the top surface, which was likely due to the enhanced surface nucleation as a result of radiative and evaporative heat losses.



**Acknowledgements**

The authors would like to thank Mr Bowen Yu for his help in microstructure characterization. They would also like to thank the UQ CIEF grant and Medical Engineering @ UQ SEED grant for financial support and acknowledge the facilities, and the scientific and technical assistance, of the Australian Microscopy & Microanalysis Research Facility at the Centre for Microscopy and Microanalysis (CMM), The University of Queensland.

**References:**

[1]. Dobrovinskaya, E.R., L.A. Lytvynov, and V. Pishchik, *Sapphire: material, manufacturing, applications*. 2009: Springer Science & Business Media.

[2]. Hagedorn, Y.-C., *Additive manufacturing of high performance oxide ceramics via selective laser melting*. 2013, Fraunhofer-Institut für Lasertechnik-ILT.

[3]. Balla, V.K., S. Bose, and A. Bandyopadhyay, *Processing of bulk alumina ceramics using laser engineered net shaping.* International Journal of Applied Ceramic Technology, 2008. **5**(3): p. 234-242.

[4]. Ozer, I., et al., *Anisotropic sintering shrinkage in alumina ceramics containing oriented platelets.* Journal of the American Ceramic Society, 2006. **89**(6): p. 1972-1976.

[5]. Huang, H. and Y. Liu, *Experimental investigations of machining characteristics and removal mechanisms of advanced ceramics in high speed deep grinding.* International Journal of Machine Tools and Manufacture, 2003. **43**(8): p. 811-823.

[6]. Li, Y., et al., *Additive manufacturing of alumina using laser engineered net shaping: effects of deposition variables.* Ceramics International, 2017. **43**(10): p. 7768-7775.

[7]. Yap, C., et al., *Review of selective laser melting: Materials and applications.* Applied Physics Reviews, 2015. **2**(4): p. 041101.

[8]. Kruth, J.-P., et al., *Consolidation phenomena in laser and powder-bed based layered manufacturing.* CIRP Annals-Manufacturing Technology, 2007. **56**(2): p. 730-759.

[9]. Niu, F., et al., *Rapid Fabrication of Eutectic Ceramic Structures by Laser Engineered Net Shaping.* Procedia CIRP, 2016. **42**: p. 91-95.

[10]. Juste, E., et al., *Shaping of ceramic parts by selective laser melting of powder bed.* Journal of Materials Research, 2014. **29**(17): p. 2086-2094.

[11]. Deckers, J., et al., *Direct selective laser sintering/melting of high density alumina powder layers at elevated temperatures.* Physics Procedia, 2014. **56**: p. 117-124.

[12]. Wilkes, J., et al., *Additive manufacturing of $ZrO_2$-$Al_2O_3$ ceramic components by selective laser melting.* Rapid Prototyping Journal, 2013. **19**(1): p. 51-57.

[13]. Yadroitsev, I., et al., *Energy input effect on morphology and microstructure of selective laser melting single track from metallic powder.* Journal of Materials Processing Technology, 2013. **213**(4): p. 606-613.

[14]. Raghavan, N., et al., *Numerical modeling of heat-transfer and the influence of process parameters on tailoring the grain morphology of IN718 in electron beam additive manufacturing.* Acta Materialia, 2016. **112**: p. 303-314.

[15]. Li, C., Y. Guo, and J. Zhao, *Interfacial Phenomena and Characteristics between the Deposited Material and Substrate in Selective Laser Melting Inconel 625.* Journal of Materials Processing Technology, 2017.

[16]. Beese, A.M. and B.E. Carroll, *Review of mechanical properties of Ti-6Al-4V made by laser-based additive manufacturing using powder feedstock.* Jom, 2016. **68**(3): p. 724-734.

[17]. Yadroitsev, I., et al., *Factor analysis of selective laser melting process parameters and geometrical characteristics of synthesized single tracks.* Rapid Prototyping Journal, 2012. **18**(3): p. 201-208.

[18]. ASTM, E.-. *112–96. Standard Test Methods for Determining Average Grain Size.* ASTM International, 2004.

[19]. Li, Y. and D. Gu, *Parametric analysis of thermal behavior during selective laser melting additive manufacturing of aluminum alloy powder.* Materials & Design, 2014. **63**: p. 856-867.

[20]. Lisitsyn, A.V., et al., *Near-infrared optical properties of a porous alumina ceramics produced by hydrothermal oxidation of aluminum.* Infrared Physics & Technology, 2016. **77**: p. 162-170.

[21]. Li, J., L. Li, and F. Stott, *Comparison of volumetric and surface heating sources in the modeling of laser melting of ceramic materials.* International Journal of Heat and Mass Transfer, 2004. **47**(6): p. 1159-1174.

[22]. Gladush, G.G. and I. Smurov, *Mechanisms of Laser Processing of Metal Surfaces*, in *Physics of Laser Materials Processing: Theory and Experiment*. 2011, Springer Berlin Heidelberg: Berlin, Heidelberg. p. 45-143.

[23]. Yuan, P., D. Gu, and D. Dai, *Particulate migration behavior and its mechanism during selective laser melting of TiC reinforced Al matrix nanocomposites.* Materials & Design, 2015. **82**: p. 46-55.

[24]. Sih, S.S. and J.W. Barlow, *The prediction of the emissivity and thermal conductivity of powder beds.* Particulate Science and Technology, 2004. **22**(4): p. 427-440.

[25]. Doremus, R.H., *Alumina*, in *Ceramic and Glass Materials: Structure, Properties and Processing*, J.F. Shackelford and R.H. Doremus, Editors. 2008, Springer US: Boston, MA. p. 1-26.

[26]. MW Jr, C., *NIST-JANAF Thermochemical Tables.* J. Phys. Chem. Ref. Data. Monograph, 1998(9).

[27]. Zhang, P., et al., *The melting point, latent heat of solidification, and enthalpy for both solid and liquid α-$Al_2O_3$ in the range 550–2400 K.* International Journal of Thermophysics, 1986. **7**(4): p. 811-819.

[28]. Yan, Y., et al., *Experimental and theoretical investigation of fibre laser crack-free cutting of thick-section alumina.* International Journal of Machine Tools and Manufacture, 2011. **51**(12): p. 859-870.

[29]. Lawrence, J., *An analysis of the beam interaction characteristics of selected lasers with an alpha-alumina bioceramic.* Optics and lasers in engineering, 2004. **41**(3): p. 505-514.

[30]. Hussey, R.J. and J. Wilson, *Advanced Technical Ceramics Directory and Databook*. 2012: Springer Science & Business Media.

[31]. Kirshenbaum, A. and J. Cahill, *The density of liquid aluminium oxide.* Journal of Inorganic and Nuclear Chemistry, 1960. **14**(3): p. 283-287.

[32]. Harimkar, S.P., A.N. Samant, and N.B. Dahotre, *Temporally evolved recoil pressure driven melt infiltration during laser surface modifications of porous alumina ceramic.* Journal of Applied Physics, 2007. **101**(5): p. 054911.

[33]. Li, Y., et al., *Heat transfer and phase transition in the selective laser melting process.* International Journal of Heat and Mass Transfer, 2017. **108**: p. 2408-2416.

[34]. Dai, D. and D. Gu, *Thermal behavior and densification mechanism during selective laser melting of copper matrix composites: simulation and experiments.* Materials & Design, 2014. **55**: p. 482-491.

[35]. Atanasov, P., E. Eugenieva, and N. Nedialkov, *Laser drilling of silicon nitride and alumina ceramics: A numerical and experimental study.* Journal of Applied Physics, 2001. **89**(4): p. 2013-2016.

[36]. Modest, F., *Temperature-Dependent Absorptances of Ceramics for Nd: YAG and $CO_2$ Laser Processing Applications.* 1998.

[37]. Lippold, J.C., *Welding Metallurgy Principles.* Welding Metallurgy and Weldability, 2015: p. 9-83.

[38]. Blecher, J., T. Palmer, and T. DebRoy, *Solidification map of a nickel-base alloy.* Metallurgical and Materials Transactions A, 2014. **45**(4): p. 2142-2151.

[39]. Yadroitsev, I., et al., *Single track formation in selective laser melting of metal powders.* Journal of Materials Processing Technology, 2010. **210**(12): p. 1624-1631.

[40]. Gusarov, A., et al., *Heat transfer modelling and stability analysis of selective laser melting.* Applied Surface Science, 2007. **254**(4): p. 975-979.

[41]. Yan, W., et al., *Multi-physics modeling of single/multiple-track defect mechanisms in electron beam selective melting.* Acta Materialia, 2017.

[42]. Paradis, P.-F. and T. Ishikawa, *Surface tension and viscosity measurements of liquid and undercooled alumina by containerless techniques.* Japanese journal of applied physics, 2005. **44**(7R): p. 5082.

[43]. Xia, M., et al., *Porosity evolution and its thermodynamic mechanism of randomly packed powder-bed during selective laser melting of Inconel 718 alloy.* International Journal of Machine Tools and Manufacture, 2017. **116**: p. 96-106.

[44]. Park, C.W. and D.Y. Yoon, *Effects of $SiO_2$, $CaO_2$, and MgO additions on the grain growth of alumina.* Journal of the American ceramic society, 2000. **83**(10): p. 2605-2609.

[45]. Khangar, A.A., E.A. Kenik, and N.B. Dahotre, Microstructure and microtexture in laser-dressed alumina grinding wheel material. Ceramics International, 2005.31(4): p. 621-629.

[46]. Shieh, J.H. and S.T. Wu, *Rapid solidification of a plasma-sprayed ceramic coating melted by a $CO_2$ laser.* Applied physics letters, 1991. **59**(12): p. 1512-1514.

[47]. Kurz, W., C. Bezencon, and M. Gäumann, *Columnar to equiaxed transition in solidification processing.* Science and technology of advanced materials, 2001. **2**(1): p. 185-191.

[48]. Gaida, N.A., et al., *Synthesis of $Al_2O_3/SiO_2$ nano-nano composite ceramics under high pressure and its inverse Hall–Petch behavior.* Journal of the American Ceramic Society, 2017. **100**(1): p. 323-332.

[49]. Li, L., *The advances and characteristics of high-power diode laser materials processing.* Optics and Lasers in Engineering, 2000. **34**(4): p. 231-253.

[50]. Kennedy, E., G. Byrne, and D.N. Collins, *A review of the use of high power diode lasers in surface hardening.* Journal of Materials Processing Technology, 2004. **155-156**: p. 1855-1860.

[51]. Harimkar, S. and N. Dahotre, *Effect of laser fluence on surface microstructure of alumina ceramic.* Advances in applied ceramics, 2006. **105**(6): p. 304-308.

[52]. Gusarov, A. and J.-P. Kruth, *Modelling of radiation transfer in metallic powders at laser treatment.* International Journal of Heat and Mass Transfer, 2005. **48**(16): p. 3423-3434.

[53]. Gusarov, A., et al., *Normal-directional and normal-hemispherical reflectances of micron-and submicron-sized powder beds at 633 and 790 nm.* Journal of applied physics, 2006. **99**(11): p. 113528.

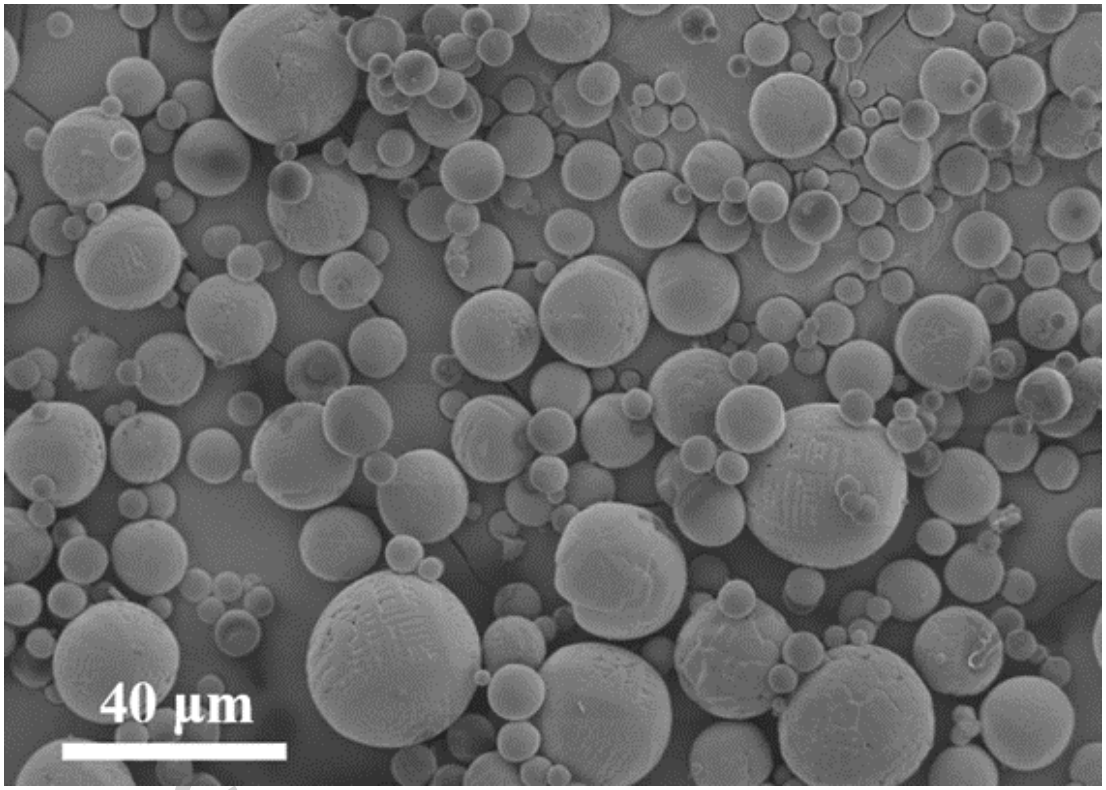


Fig 1 The SEM image of the $Al_2O_3$ powder

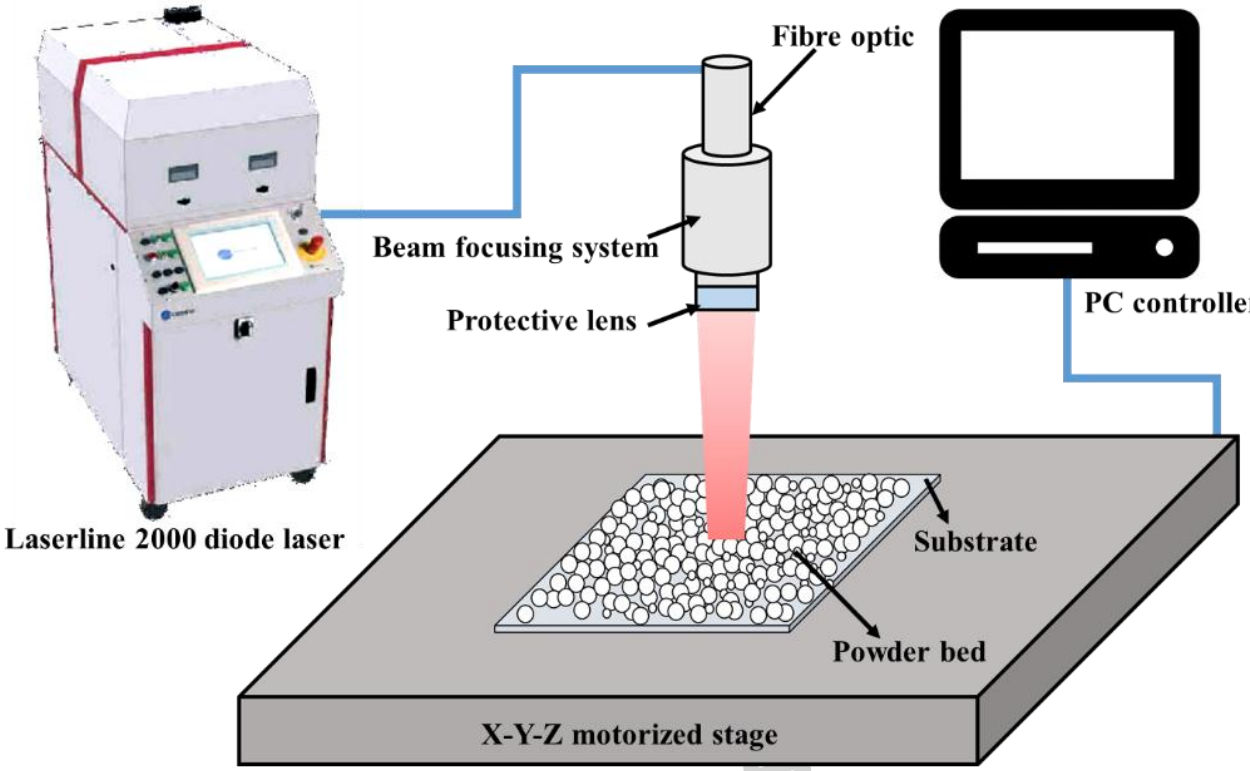


Fig 2 The schematic of the customised SLM system

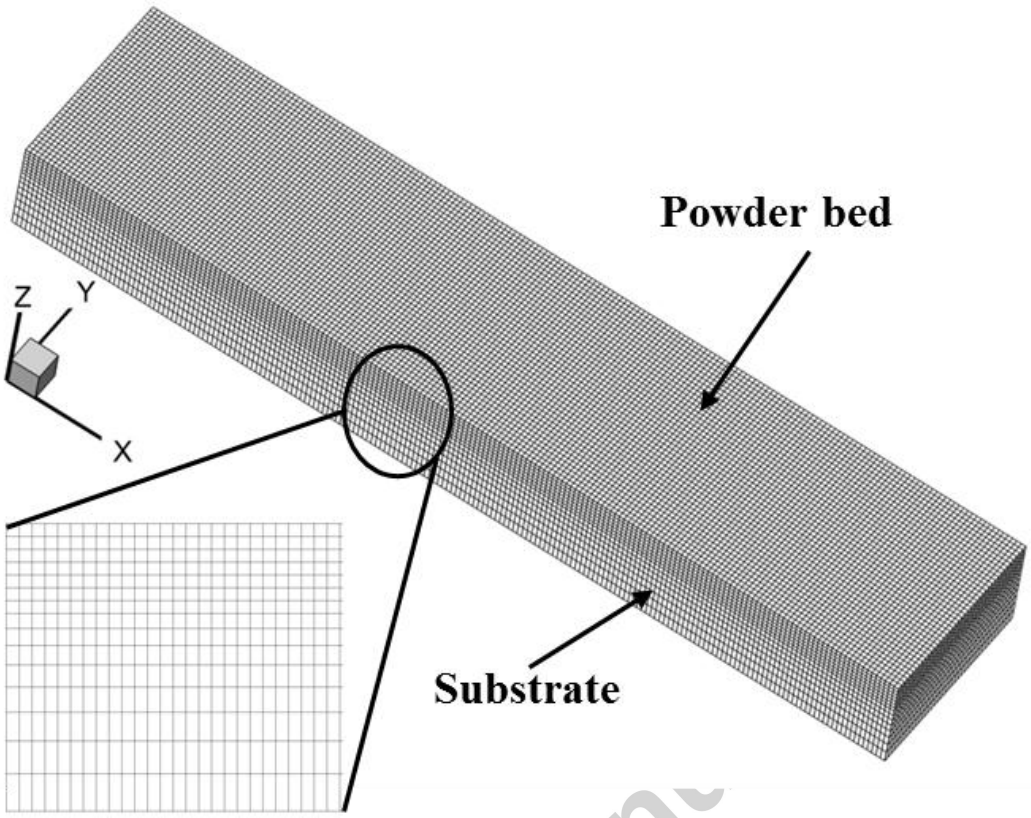


Fig 3 The meshed powder-substrate structure in the FVM model

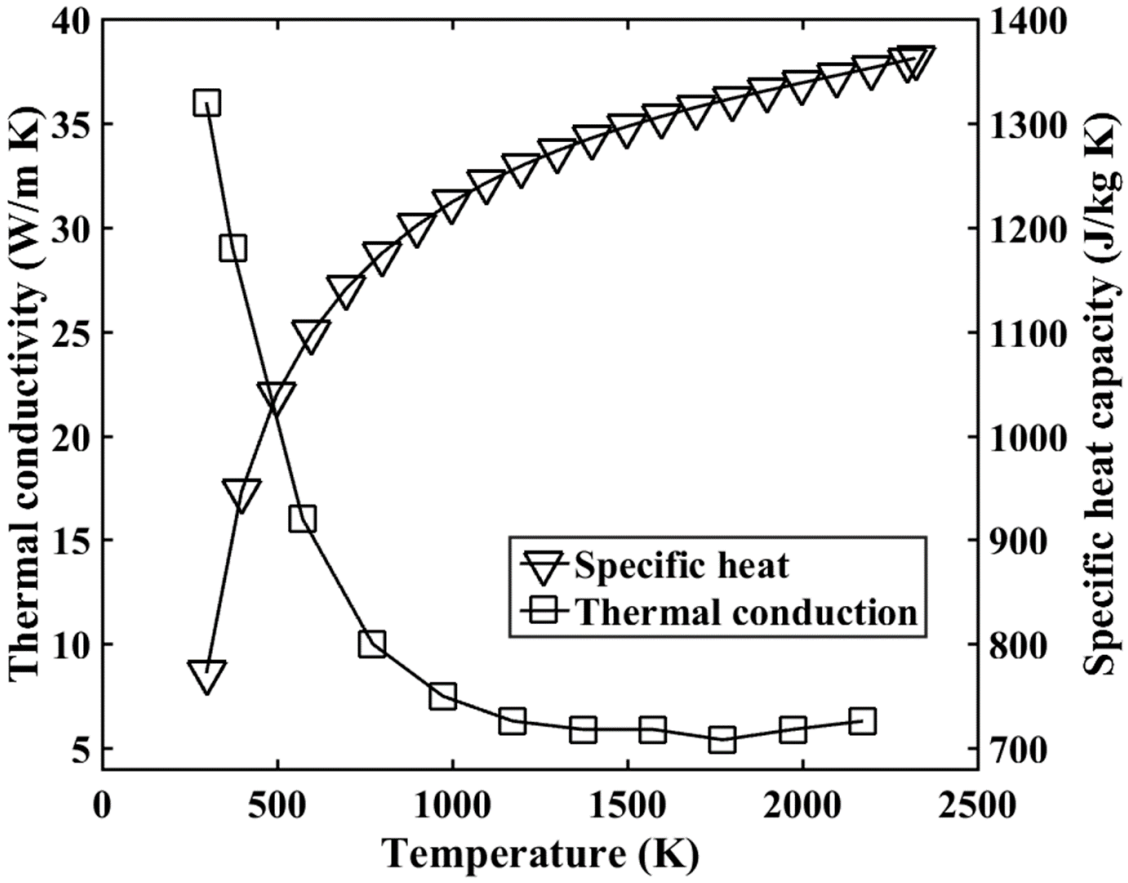


Fig 4 Thermal conductivity and specific heat of bulk alumina plotted as a function of temperature [25, 26]

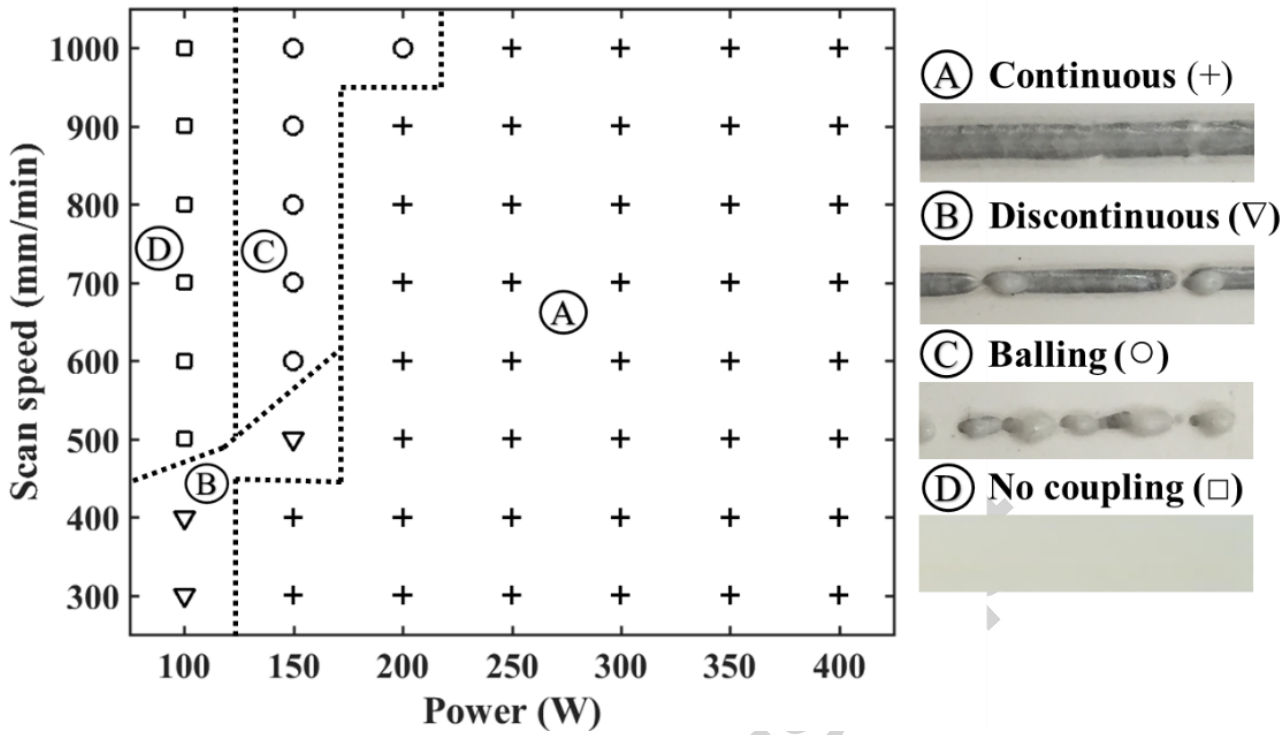


Fig 5 The SLM process map for $Al_2O_3$ single tracks

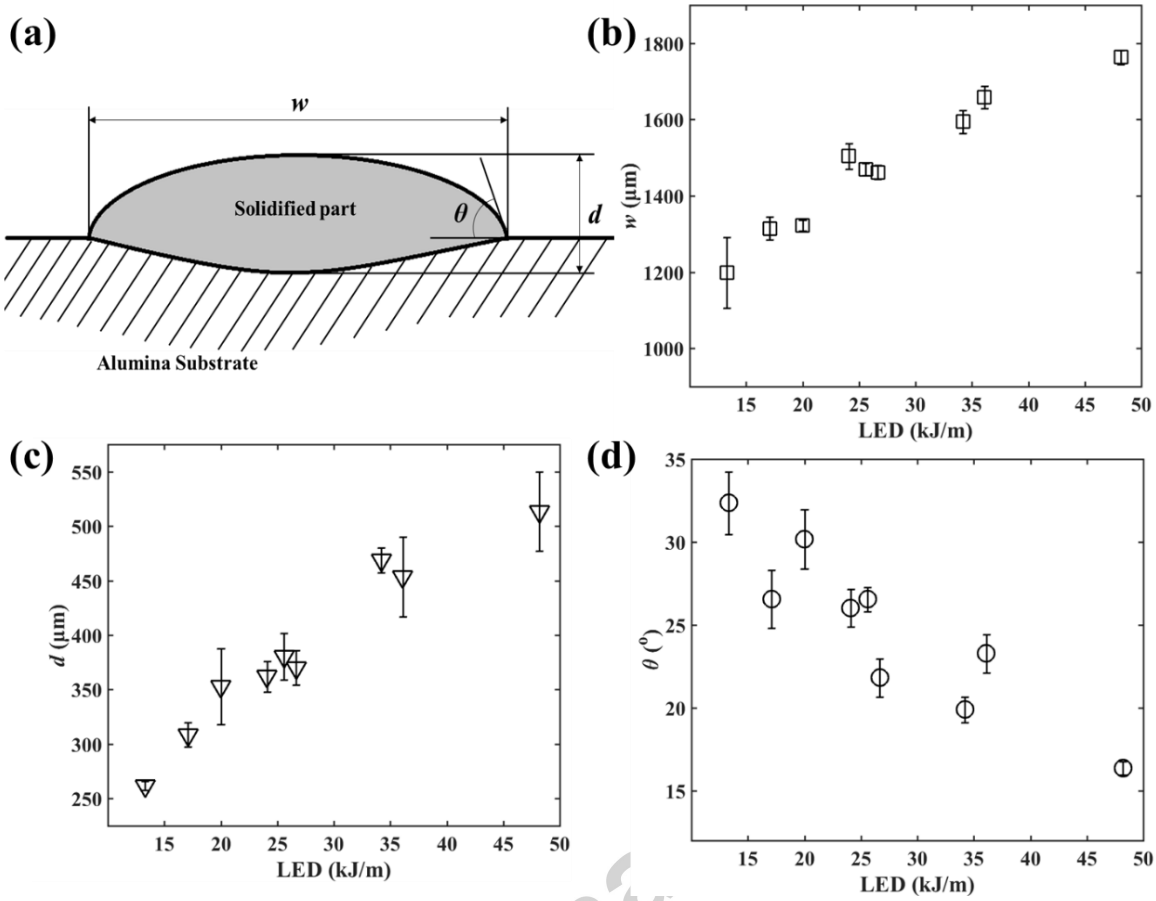


Fig 6 (a) The cross-sectional view of typical single tracks and track (b) width *w*, (c) depth *d* and (d) contact angles *θ* plotted as a function of the magnitude of LED

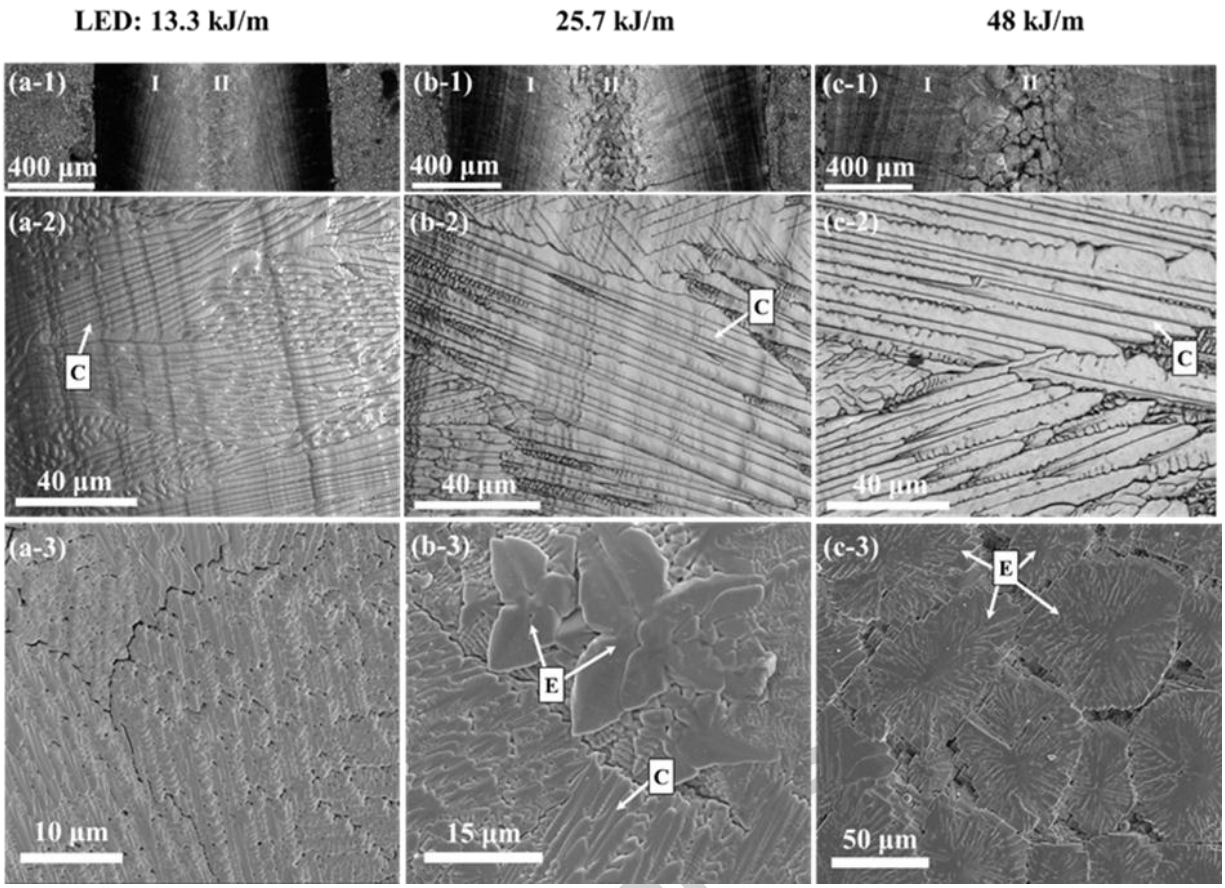


Fig 7 Top surface microstructure of single tracks formed using different processing parameters: (a) 13.3 kJ/m, 200 W, 900 mm/min, (b) 25.7 kJ/m, 300W, 700 mm/min and (c) 48 kJ/m, 400W, 500 mm/min. For each track in (a), (b) and (c), high magnification images of the area within the tracks adjacent to the edge (I) are shown in (a-2), (b-2) and (c-2), respectively, in which columnar dendrites (C) populate and high magnification images of the centre of the tracks (II) are shown in (a-3), (b-3) and (c-3), respectively, in which a transition from columnar dendrites to equiaxed dendritic grains (E) was found.

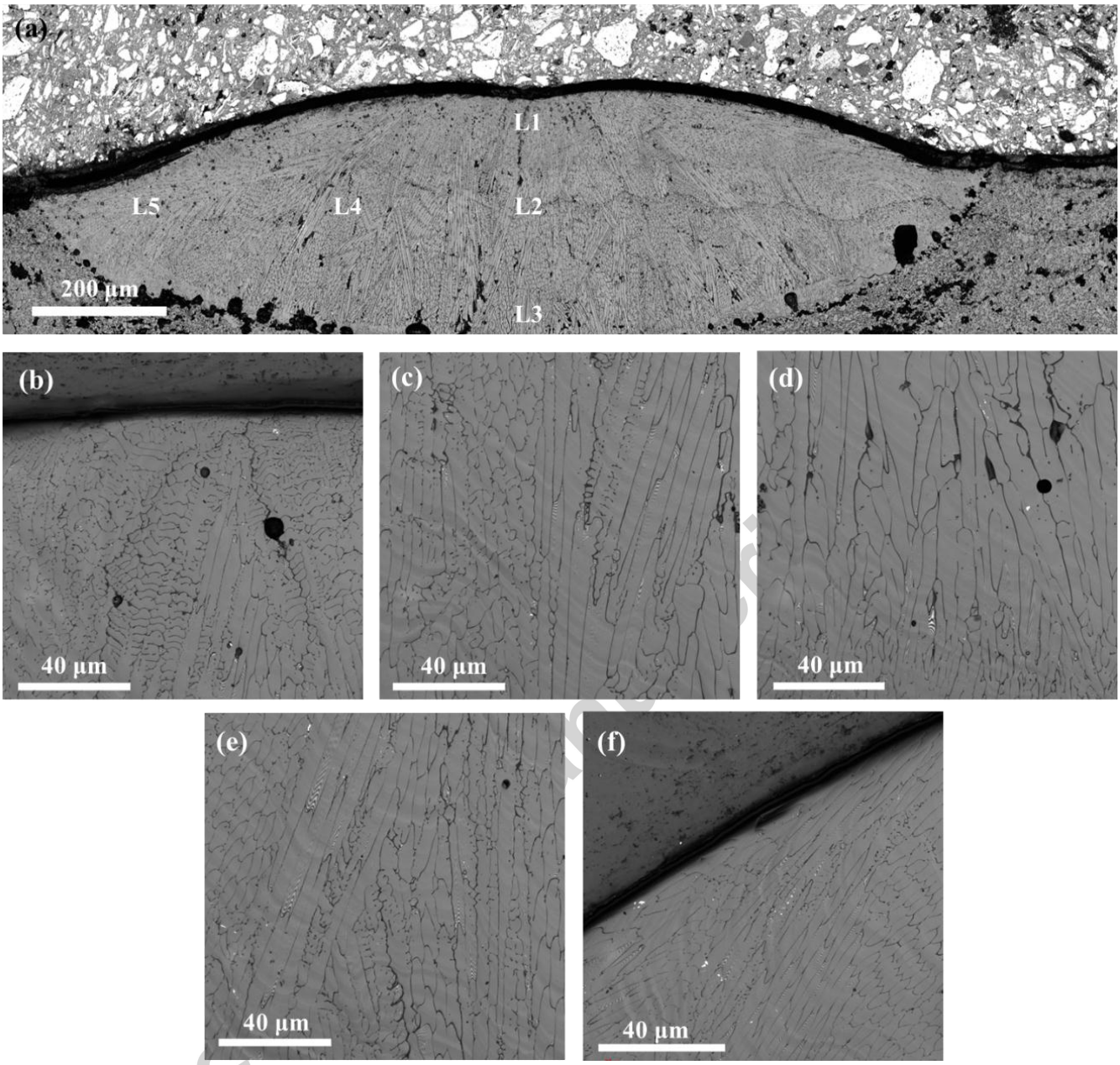


Fig 8 (a) Cross-sectional image of a single track. The columnar dendrite structures. in the different zones of (a), (b) L1, (c) L2, (d) L3, (e) L4, (f) L5. ($P$ = 300 W, $v$ = 700 mm/min and LED = 25.7 kJ/m)

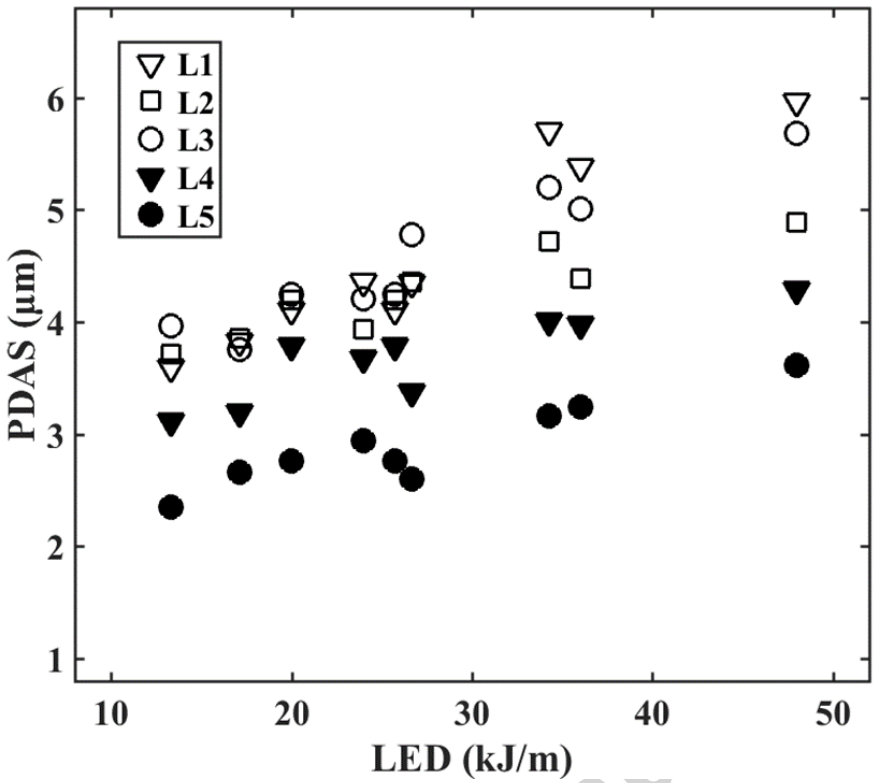


Fig 9 PDAS of columnar dendrites plotted as a function of the magnitude of LED

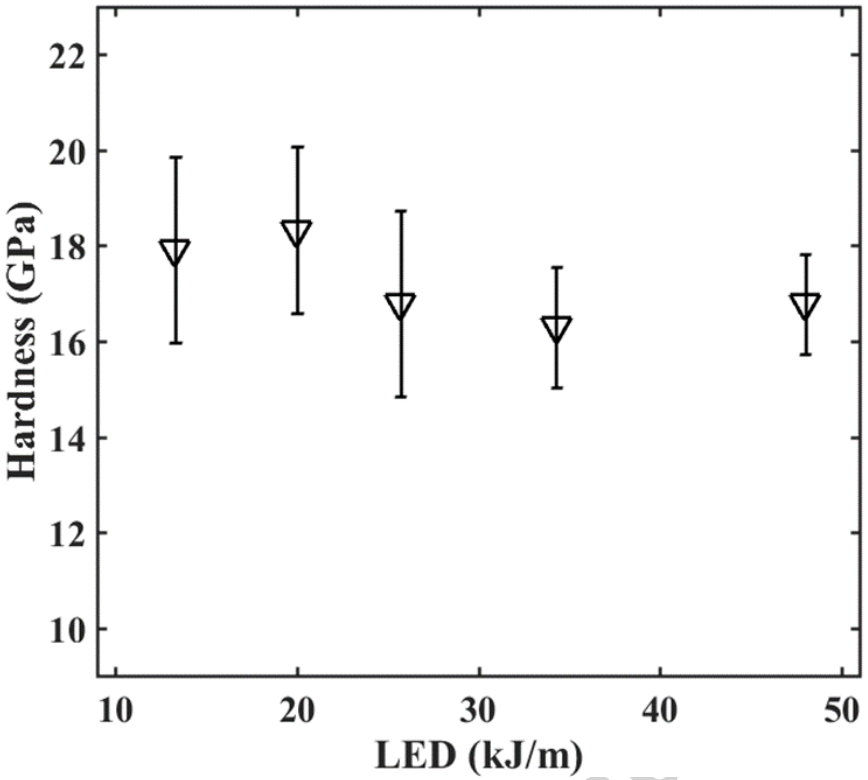


Fig 10 Microhardness of SLM single track plotted as a function of the magnitude of LED

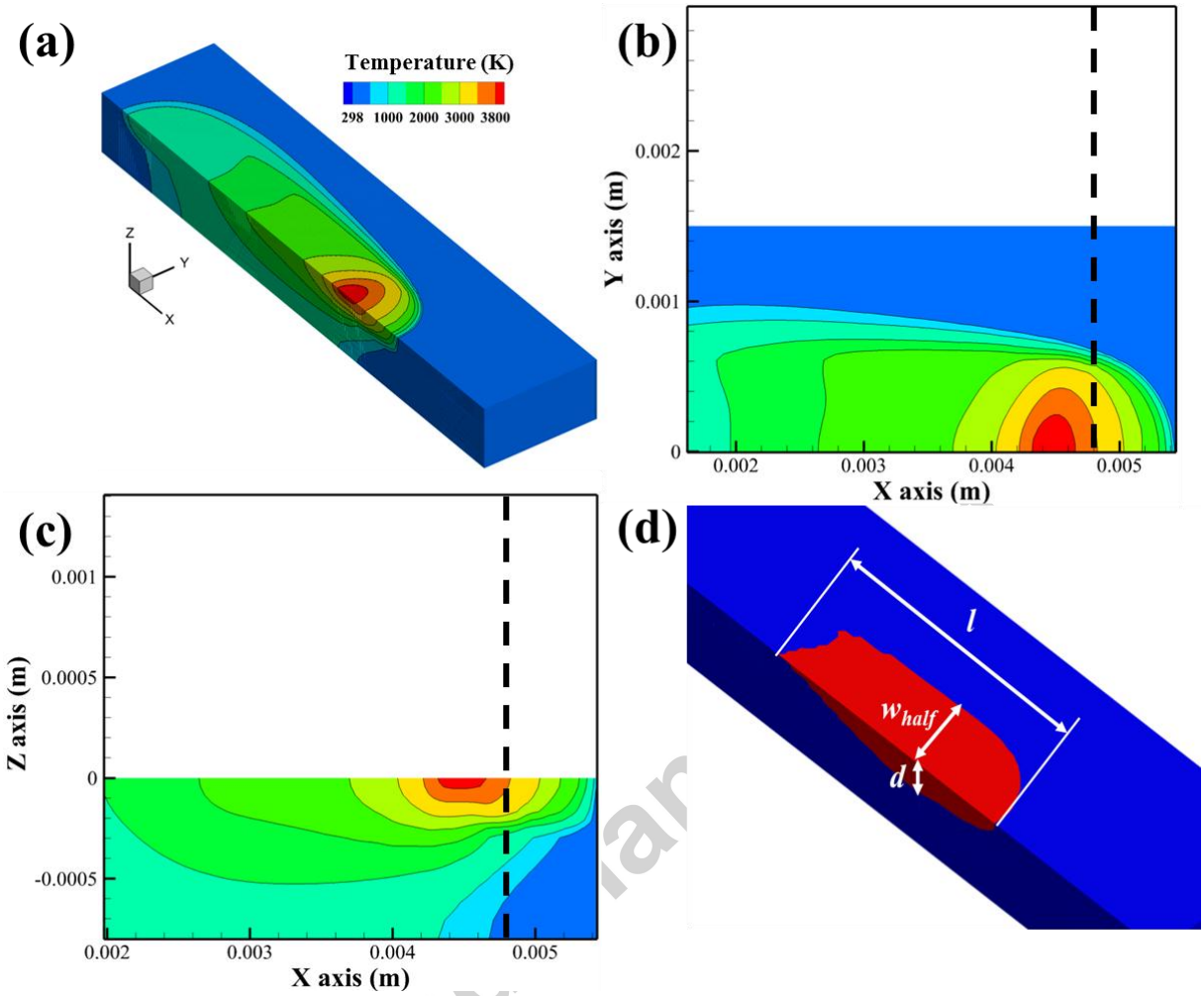


Fig 11 (a) The 3D profile of transient temperature distribution in a typical melt pool ($P$=300 W, $v$ = 700 mm/min, LED = 25.7 kJ/m) and the temperature coutours of (b) x-y and (c) x-z planes. (d) The geometry of the molten pool captured from isothermal line (2327 K)

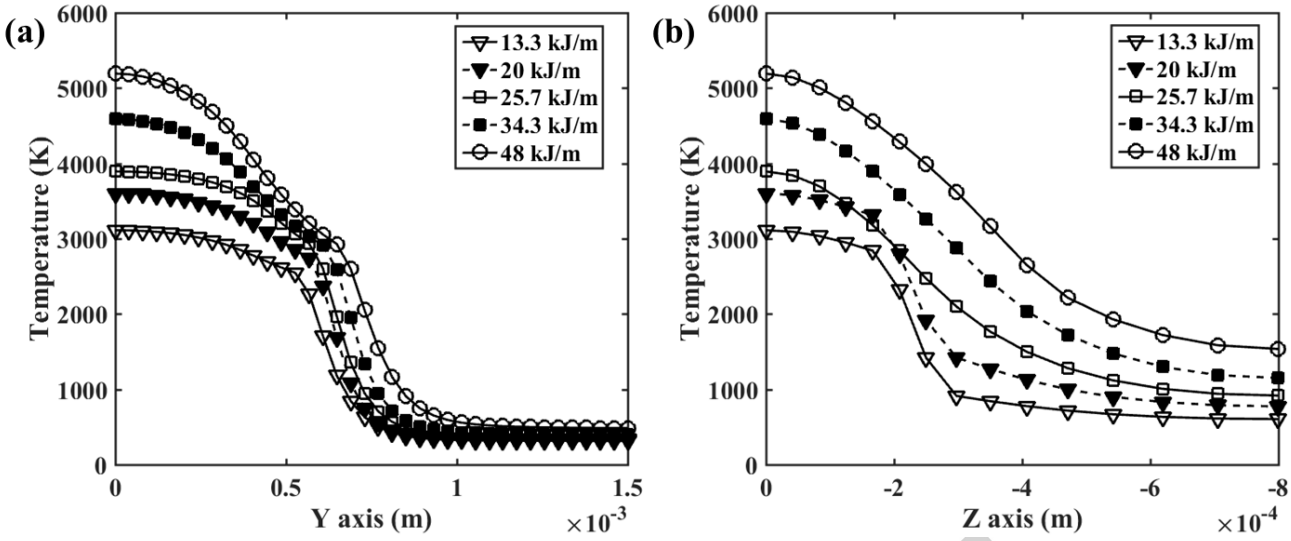


Fig 12 Temperature variation along (a) y axis (surface) and (b) z axis (subsurface)for different values of LED. The origins of all curves (at y = 0, z = 0) are coincident with the temperature maxima.

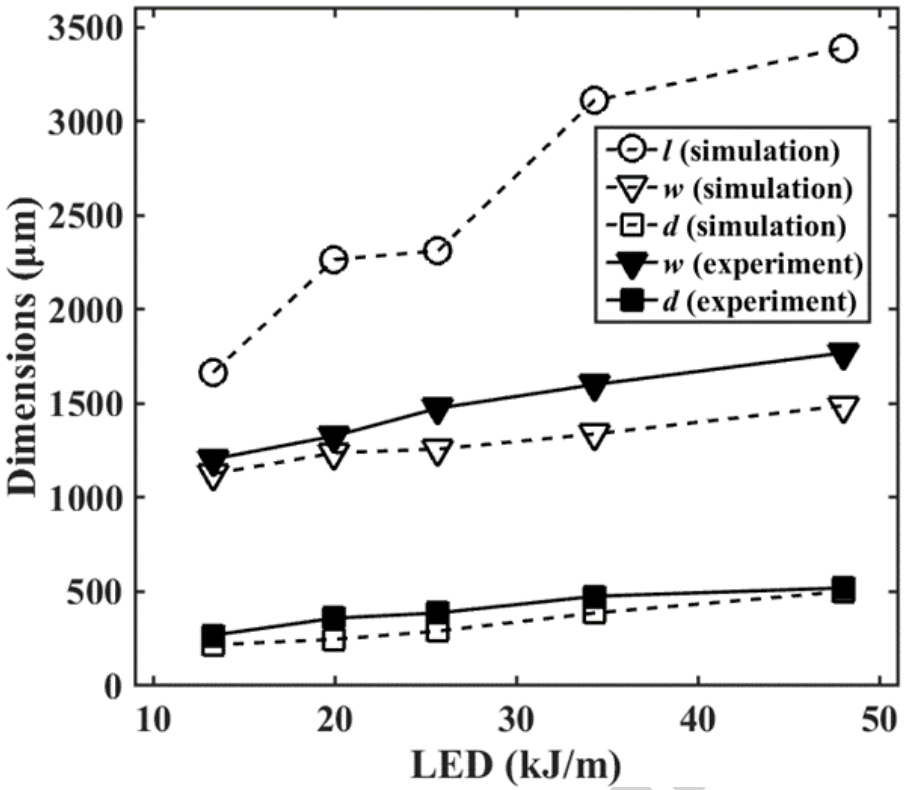


Fig 13 Comparison of simulated and experimentally measured dimensions of the molten pools obtained from different LEDs

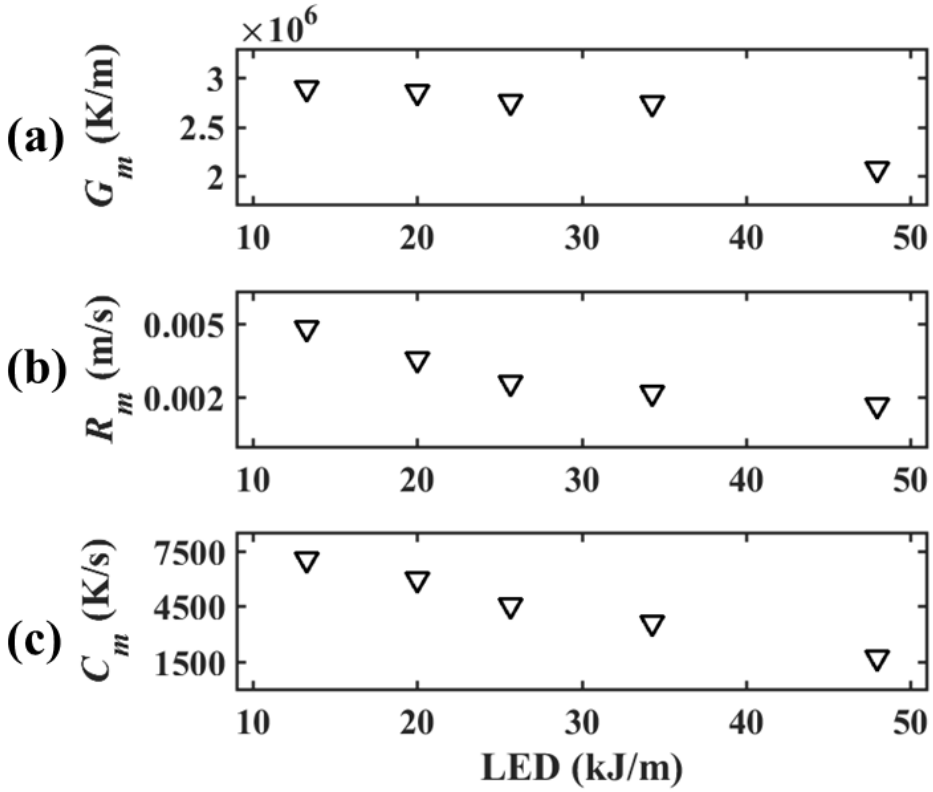


Fig 14 Values of solidification parameters (a) $G_m$, (b) $R_m$ and (c) $C_m$ plotted as a function of the magnitude of LED

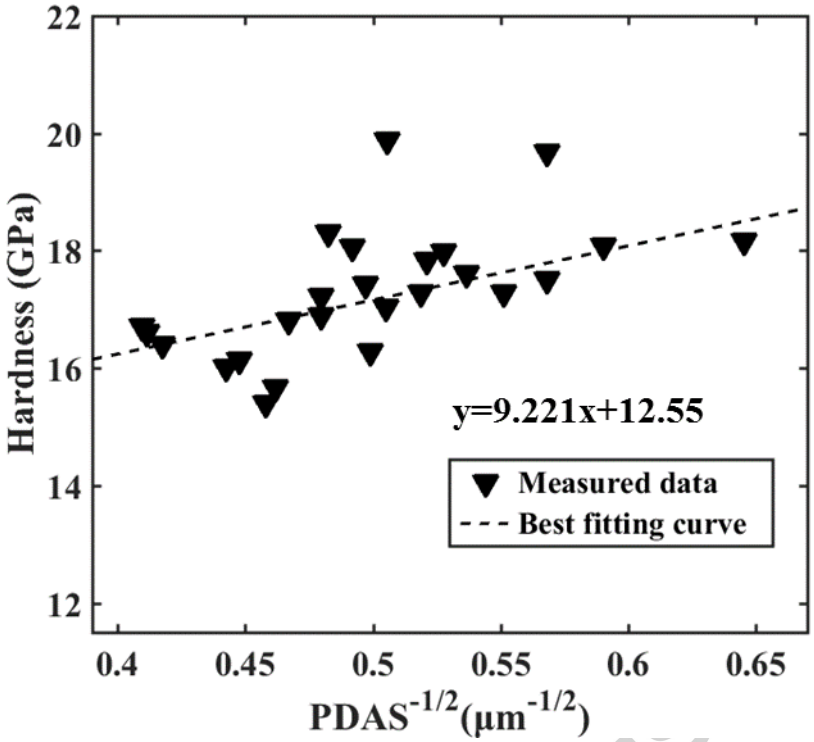


Fig 15 Microhardness plotted as a function of inverse square root of PDAS (primary dendrite arm spacing)

Table 1 The physical properties of $Al_2O_3$ used in simulation

| Property | Value | Reference |
|---|---|---|
| Melting point | 2327 K | [27] |
| Reflectivity | 0.79 | [28] |
| Absorption coefficient | 110.28 $cm^{-1}$ | [29] |
| Powder material density | 1580 $kg/m^3$ | Measured |
| Solid material density | 3950 $kg/m^3$ | [30] |
| Liquid material density | 2800 $kg/m^3$ | [31] |
| Porosity | 0.6 | Measured |
| Latent heat of melting | 1137900 J/kg | [27] |
| Emissivity | 0.7 | [32] |
| Stefan-Boltzmann constant | $5.6704e^{-8}$ $W/m^2 K^4$ | [33] |
| Thermal convection coefficient | 200 $W/m^2 K^4$ | [32] |